Physics of Fluids 31, 107107 (2019);
https://doi.org/10.1063/1.5115351

Flutter-Enhanced Mixing in Small-Scale Mixers

Aaron Rips & Rajat Mittal
Department of Mechanical Engineering, Johns Hopkins University, Baltimore, Maryland, 21218

1 Abstract

Enhancement of mixing via flow-induced flutter of a flexible membrane is explored for small-scale mixers that operate at low Reynolds numbers. Flow induced flutter and mixing in a duct flow is simulated using fully coupled fluid-structure-scalar interaction simulations including two-way coupling between the fluid and structure. The fluid and structural dynamics are analyzed and their impact on the mixing performance is characterized. The sensitivity of the system to Reynolds number and to the membrane's size and shape are also examined. It is shown that these flutter mixers create complex vortex structures even at low Reynolds numbers and these vortex structures lead to complex stretching and folding of fluid interfaces resulting in rapid mixing.

2 Introduction

Mixing in small (mm to cm) scale mixers is of interest in a variety of scientific, medical, and industrial fields and applications. Applications include technologies such as lab-on-a-chip (LOC) devices, micro-total-analysis systems (μTAS), small-scale bioreactors and electronic cooling (Cai et al., 2017; Capretto et al., 2011; Lee et al., 2011; Lee et al., 2016; Nguyen & Wu, 2004; Stone, Stroock, & Ajdari, 2004; Zhang et al., 2016). In many of these applications, the small size and low flow rates result in low Reynolds numbers (100 or lower). This coincides with the so-called inertial microfluidic regime (Amini, Lee, & Di Carlo, 2014) where molecular diffusion is limited and turbulence-induced mixing is not available. Thus, other novel approaches are needed to enhance mixing in such devices.

Mixers can be broadly categorized as either active or passive. Active mixers utilize some sort of external energy or control, whereas passive mixers are limited to only the energy provided by the flow (Nguyen & Wu, 2004). While active mixers come in a wide variety of forms (rotors, acoustic/electromagnetic actuation, etc.), in principle, they all operate by introducing temporal fluctuations into the flow to enhance mixing by stretching and folding the interface between the fluids. This approach typically leads to very strong mixing performance but at the cost of significant system complexity. In contrast, passive mixers in this regime cannot introduce significant temporal variations as the Reynolds number is too low to achieve passive vortex shedding in a confined duct. Instead, mixing enhancement is achieved through various mechanisms such as the use of complex duct shapes (Afzal & Kim, 2012; Hossain, Ansari, & Kim, 2009; Lee et al., 2016) that introduce spatial variations in interfaces which increase the interface length between the fluids to enhance molecular diffusion.

The idea behind this work is to investigate a hybrid approach; a passive mixer that can introduce temporal fluctuations into the fluid even at inertial-scale Reynolds numbers. This is done by introducing a flexible membrane (or flag) in the duct. An appropriately chosen membrane undergoes flow-induced flutter thereby leading to temporal and spatial fluctuation in the flows. The mechanism we investigate to accomplish this task is the flow induced flutter of flexible membranes.

Rips & Mittal (2019) employed two-dimensional (2D) simulations to examine the mixing performance of such a flutter mixer. In that work, it was shown that for a particular set of parameters these membranes

could flap at Reynolds numbers (based on channel height) as low as 15, with evidence to suggest that a broader range of structural parameters would yield even lower critical Reynolds numbers. However, this earlier 2D modeling study excluded any three-dimensional effects which may be significant for such applications. Flow passages in these mixers tend to be compact (aspect-ratio of O(1)) where the flow is highly three-dimensional. In addition, Eloy et. al., (2008) have shown that finite-span effects make membranes more stable to flutter than 2D (infinite span) membranes, and work by Doare et. al., (2011) showed that spanwise confinement effects intrinsic to a 3D membrane in a duct flow also lead to increased stability, i.e. a higher critical Re numbers for flapping. More recent work has focused on the effect of cross-stream confinement on flapping membranes on stability and mode shapes (Alben, 2015). Other recent work has investigated energy extraction from the flapping membrane (Shoele & Mittal, 2016; Wang et al., 2016). Finally, prior work (Huang & Sung, 2010; Rips et al., 2017) has shown 3D membranes shed very different vortical structures than 2D filaments and this could have significant implications on the mixing downstream of the membrane.

The current study seeks to expand the utility and fidelity of the prior work by Rips & Mittal (2019) by examining a more realistic, three-dimensional model of this mixer. In particular, we use three-dimensional (3D) fully-coupled fluid-structure-scalar interaction simulations to examine mixing in the Reynolds number regime of O(10) – O(100) which is relevant for inertial microfluidics. We seek to understand the fluid and structural dynamics of the system to identify mechanisms that are responsible for the mixing performance in these mixers. We then examine the sensitivity of this system to Reynolds number, as well as membrane aspect ratio. This 3D analysis allows us to directly investigate the mixing mechanisms, mixing performance, and parameter sensitivities which would be important in a real-world flutter mixer.

3 Problem Configuration

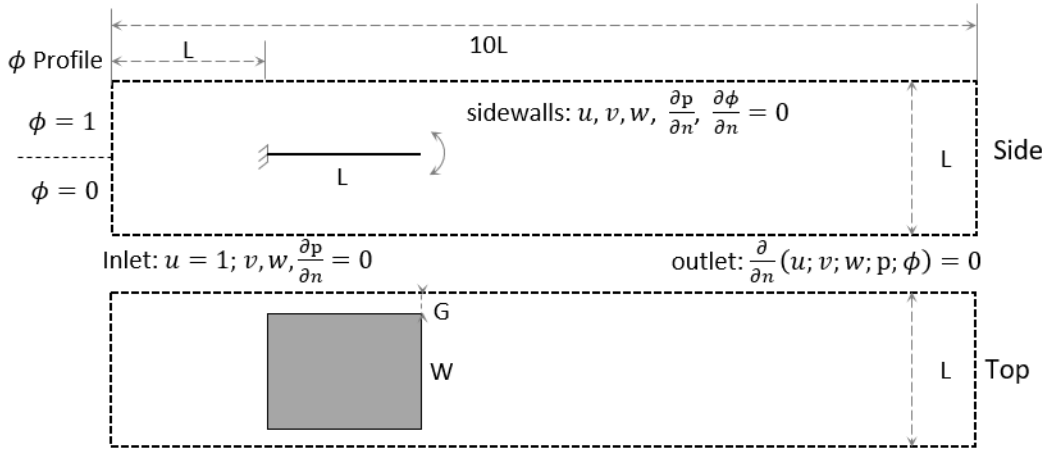

FIG. 1 – Schematic view of the 3D flutter mixer configuration. The mixer is a L x L duct of length 10L. The flag is a rectangular membrane of size L x W placed at a distance of L from the entrance of the mixer.

In the current study we consider a flapping flag installed in a square duct. FIG. 1 shows a schematic of the system depicting a side view and a top view. The rectangular flag (length L and width W) is assumed to have negligible thickness. The flag is placed near the entrance of the duct to model the flow that would be seen in a T type or Y type mixer (Nguyen & Wu, 2004). So as to properly model this channel entrance behavior, the inflow boundary condition is modeled as a uniform plug flow with U=1 where U is the velocity in the streamwise direction. The duct is considered to have no slip, no penetration boundary

conditions on the walls and the outflow is modeled with zero-gradient, convective boundary conditions which corresponds to a nonreflecting outlet boundary condition for incompressible flows which represents a channel which continues arbitrarily. The species to be mixed is modeled as a passive scalar with a normalized concentration ϕ and the inflow to the duct is a step function with ϕ = 1 in the top half of the duct and ϕ = 0 in the lower half. This inflow boundary condition is oriented such that the interface is coplanar with the membrane's surface.

3.1 Numerical Methods

This fluid-structure-scalar multiphysics system exhibits two-way coupling between the fluid and structure and one way coupling between the fluid and the scalar concentration. To compute the fluid and scalar fields as well as the structural position, we perform fully coupled 3D fluid-structure-scalar interaction simulations. The fluid is governed by the incompressible Navier-Stokes equations. The dynamics governing the position of the membrane are derived from the principle of virtual work (Huang & Sung, 2010) and are given in terms of the Lagrangian position vector $\mathbf{X}$ of the membrane. The scalar ϕ is governed by an advection-diffusion equation. The governing equations are as follows:

$$\frac{\partial \mathbf{u}}{\partial t} + \nabla \cdot (\mathbf{uu}) = -\nabla p + \frac{1}{\mathrm{Re}} \nabla^2 \mathbf{u} + \mathbf{f} \tag{1}$$

$$\nabla \cdot \mathbf{u} = 0 \tag{2}$$

$$\frac{\partial \phi}{\partial t} + \mathbf{u} \cdot \nabla \phi = \frac{1}{\mathrm{Re} \cdot \mathrm{Sc}} \nabla^2 \phi \tag{3}$$

$$\frac{\partial^2 \mathbf{X}}{\partial t^2} = \sum_{i,j=1}^{2} \left[\frac{\partial}{\partial s_i} \left(\sigma_{ij} \frac{\partial \mathbf{X}}{\partial s_j} \right) - \frac{\partial^2}{\partial s_i \partial s_j} \left(\frac{M^*}{U^{*2}} \frac{\partial^2 \mathbf{X}}{\partial s_i \partial s_j} \right) \right] - \mathbf{F} \tag{4}$$

In the fluid governing equations (1) and (2), $\mathbf{u}$ is the velocity field, t is time, p is pressure, Re is the Reynolds number defined as $\mathrm{Re} = UL/\nu$ where *U* is the mean inlet velocity, L is the characteristic length given by the length of the membrane, and ν is the dynamic viscosity of the fluid. $\mathbf{f}$ is a forcing function associated with the fluid-structure interaction penalty method and is the projection of the force density on the structure onto the fluid field via a delta function according to $\mathbf{f}(\mathbf{x},t) = \int \mathbf{F}(s,t)\delta\left[\mathbf{x} - \mathbf{X}(s,t)\right] ds$. For the scalar equation (3), ϕ is the scalar concentration and Sc is the Schmidt number defined as $\mathrm{Sc} = \nu/\mathrm{D}$ where D is the mass diffusivity of the scalar species. Equation (4) governs the position of the membrane where σ is tension. The key non-dimensional parameters governing the structure are the mass ratio M^* and reduced velocity U^*:

$$M^* = \frac{\rho L}{m_s}, \qquad U^* = UL\sqrt{\frac{m_s}{k_b}} \tag{5}$$

where k_b is the bending rigidity and m_s is the excess mass per unit area. These two values are held fixed throughout the study at the following values: *M** = 0.5 and *U** = 15. This choice is based on our previous 2D simulation studies (Shoele & Mittal, 2014; Rips & Mittal, 2019) which showed large flapping amplitudes for these parameter values. These values can be realized by choosing appropriate materials such as a variety of plastics, synthetic polymers, and metals, and they result in large-amplitude flutter.

In equation (4), $\mathbf{F}$ is the force density induced by the element on the surrounding fluid associated with the penalty forcing method used to couple the fluid and the structure solutions. That penalty method is described in prior work (Huang & Sung, 2010; Shoele & Zhu, 2012; Shoele & Mittal, 2014), but as an abbreviated explanation, the coupling force is calculated by creating a set of virtual, massless, fluid following points which are advected according to the local fluid velocity at any given timestep. Those points are then connected back to the Lagrangian structure points via spring-damper "connectors" and the force in those connectors becomes the penalty coupling force according to:

$$\mathbf{F}(s,t) = -\kappa_p \frac{\rho U^2}{L}\Big[\Big(\tag{6}$$

where κ_p and β are the penalty parameters, and Δt is the computational time step. Here, the expression for F essentially describes restoring forces which has a term proportional to position (analogous to a spring) and a term proportional to velocity (analogous to a damper). Based on a prior sensitivity analysis (Shoele & Mittal, 2016), these parameters were chosen as $K_p = -10^5$, $\beta = 150$, and $dt = 1.0 \times 10^{-4}$. The governing equations are solved using the in-house code ViCar3D which uses a second-order fractional step method on semi-staggered Cartesian grids (Mittal et al., 2008). The 2nd-order Crank-Nicolson fully implicit scheme is used for the convective and diffusion terms and the pressure Poisson equation is solved with the biconjugate gradient (BiCGSTAB) scheme (Zhu et al., 2017). Further details of the method can be found in Mittal et al., (2008) and Seo et al., (2011) and validation and benchmarking for flow-induced flutter problems can be found in prior work using this solver (Shoele & Zhu, 2012; Shoele & Mittal, 2014).

The fluid and scalar governing equations in the current study are solved on a uniform Cartesian grid in a 10*L* x *L* x *L* domain with *dx=dy=dz*=0.01L resulting in 960x96x96 grid points. Uniform grids were required to resolve the strong gradients in the scalar field at these Peclet numbers. The membrane grid employs 128 points/L, which provides high resolution for the structural dynamics. This grid size has been chosen based on our previous 2D studies. A grid convergence analysis was conducted for a selected baseline case with Re=200, Sc=100 wherein the resolution was increased in each direction by a factor of 1.33 to a 1280x128x128 grid representing a 2.4x increase in total number of points. This case resulted in nearly identical head loss (<0.1% difference) and a less than 3% difference in the mixing index. These results indicate that the flow and structural dynamics of the flag are well converged on this grid.

3.2 Performance Measures

The performance of the system is measured with three key metrics. First is the Mixing Index (M), which is defined as:

$$M(x) = 1 - \sqrt{\frac{\sigma(x)^2}{\sigma_{\max}^2}} \tag{7}$$

$$\sigma(x) = \sqrt{\frac{1}{L^2}\int_0^Z \int_0^Y \left(\phi(x,y,z) - \overline{\phi}_m(\mathrm{x})\right)^2 dydz} \tag{8}$$

where $\sigma(x)$ is the standard deviation, ϕ is the scalar concentration, $\overline{\phi}_m$ is the mean of the field at a given x plane and $\sigma_{\max}$ is the maximum deviation in the scalar field, which occurs at the inlet. The mixing index is essentially the normalized variance of the scalar concentration. It ranges from 0 to 1 with *M*=0 indicating

totally unmixed flow and *M*=1 is completely mixed flow. We also calculate an equivalent mixing length (E_M) for each flutter mixer, which correspond to an estimated length of the duct without the flag that would result in the same level of mixing that the mixer with the flag achieves at the exit (x/L=10). The method for calculating this metric is described in the next section.

To fully understand the effectiveness of a given mixing enhancement device, the energy losses associated with the mixing mechanisms must also be considered. To quantify the losses in mechanical energy due to the mixing enhancing device, we calculate the head loss (*HL*) through the duct based on the non-dimensional head (*H**):

$$H^*(x) = \frac{H(x)}{\rho U^2} = \int_0^Z \int_0^Y \left(p(x,y,z) + \frac{1}{2}u^2(x,\mathrm{y},z) \right) dydz \tag{9}$$

$$HL^*(x) = H^*(0) - H^*(x) \tag{10}$$

where *p* is the pressure, *u* is the streamwise velocity component, and ρ is the fluid density. Following conventional approaches (Fox, Robert W.,, Pritchard, Philip J., McDonald,Alan T., 2011), we also represent the head loss as an equivalent length (E_H) of the duct without the flag.

The idea underlying all laminar-flow mixers is the elongation of fluid interfaces via stretching and folding across which, molecular diffusion can work to mix the fluid. The mixing index provides a clear measure of the mixing effectiveness, but it is a composite measure of interface lengthening as well as molecular diffusion and therefore dependent not only on the flag dynamics but also on parameters associated with molecular diffusion (i.e. Reynolds and Schmidt numbers). It would be useful to extract from our simulations a direct and distinct measure of the interface length to characterize the effects of stretching and folding induced by the flag flutter in a manner that is mostly independent of subsequent molecular diffusion effects.

3.2.1 Method for Estimating Interface Length

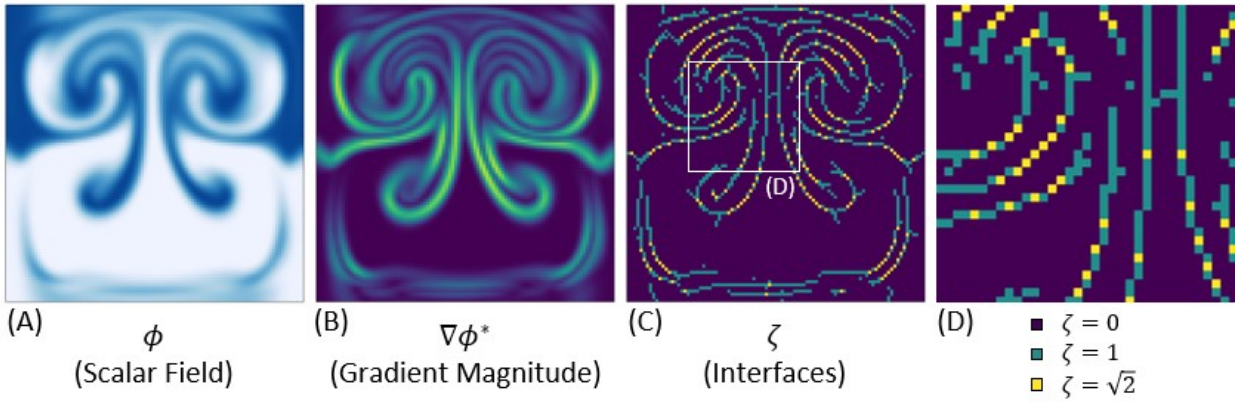

FIG. 2 – Example of the interface identification process showing (A) the scalar concentration ϕ, (B) the normalized magnitude of the scalar gradient $\nabla\phi^*$, and (C) the interface field ζ. A zoomed view of the interface field is shown in (D).

Estimation of the length of the interface between two scalar fields within a viscous unsteady flow is not straightforward. Here we generate this estimate through a multi-step postprocessing of the scalar field as described by the following procedure:

1. At each streamwise location, extract the scalar concentration field ϕ (see FIG. 2A).
2. Compute the gradient of this scalar field $\nabla\phi^*$ and generate a normalized gradient magnitude:

$$\nabla\phi^*(x,y,z) = |\nabla\phi(x,y,z)| / \|\nabla\phi(x)\|_\infty \tag{11}$$

This normalization step eliminates the diffusive effect of viscosity, which tends to reduce the magnitude of the scalar gradients as the scalar advects downstream. FIG. 2B shows the corresponding normalized gradient field. Note that local maxima of this quantity identify regions that correspond to the interfaces between the scalar field. The two scalar fields are identified by ϕ =1.0 and 0.0.

3. Identify local peaks in $\nabla\phi^*$ by scanning the data in both directions and tag grid cells where such peaks are located. FIG. 2C shows this field of cells with identified peaks.
4. Peaks that exhibit a maximum only in one direction (either y or z) are ascribed an interface length $\varsigma = \Delta = \Delta y = \Delta z$, whereas cells that exhibit a peak in both directions are ascribed an interface length equal to the diagonal of the cell, i.e. $\varsigma = \sqrt{2}\Delta$. FIG. 2D shows an inset view of the interface field with such identification.
5. The total interface length is calculated by summing the ς over the entire plane, i.e.

$$I(x_i) = \sum_{j=1}^{N_y}\sum_{k=1}^{N_z}\zeta(j,k;x_i)\,; \quad i = 1, N_x \tag{12}$$

We have assessed this method of estimating interface length for a variety of prescribed canonical scalar fields and the estimates are reasonably accurate. We estimate this interface length at each streamwise location in the mixer and present this data as an interface length normalized by the length of the interface at the inlet of the duct where the effect of the flag has not yet deformed the interface.

$$I^*(x) = I(\mathrm{x}) / I(0) \tag{13}$$

We note that $I(0) \equiv \mathrm{L}$ for the current configuration. The minimum value of this normalized interface length is 1.0 and values higher than unity indicate the degree of stretching of the interface. A good mixer should achieve a rapid and continuous increase in the interface length.

4 Results

To explore the flutter mixer, we first examine in detail a baseline case at Re=200, Sc=100 with a flag length of L and width W=0.75L. We then study the behavior of this system at Reynolds numbers of 50, 100, 150, and 200, all at Sc=100. This Reynolds number sweep is important because the applications for small-scale flutter mixers exist in the O(1)-O(100) Reynolds number regime where fluid dynamics phenomena often show strong Reynolds number dependence. In the prior 2D study (Rips & Mittal, 2019) we examined a range of Schmidt numbers (1-1000) and found that the results were quite insensitive to this parameter beyond a value of 100, and below this value, diffusive mixing became quite noticeable. As a result of this observation, and due to the computational expense associated with these 3D simulations, we examine only a single Schmidt number corresponding to Sc=100. This value of Schmidt number is high enough that convective mixing is dominant over diffusive mixing, and it is well within the range of Schmidt numbers encountered in practical applications (Nguyen & Wu, 2004). We subsequently examine the effect of flag aspect-ratio, which is a key design parameter in this device. As will be shown, the generation of vortices

from the spanwise edges of the flag plays an important role in the mixing enhancement, so it is valuable to understand how the production of this streamwise vorticity might be modified and how the behavior and interaction of that streamwise vorticity would subsequently change.

FIG. 3 shows a snapshot for the Re=200 case including vortex structures and the interface in the scalar field. We can immediately see in the scalar field how vorticity shed from the flag is responsible for mixing the flow. In FIG. 3A, examining the cross-stream plane immediately downstream of the flag, we can see a large, symmetric swirl pattern where it appears that the light-colored fluid is being forced upwards creating a jet up into the dark-colored fluid. At the center of the swirl patterns are large vortical structures as shown with the isosurfaces of the λ_2 criterion.

The streamwise vortices at the centers of these swirl patterns are the characteristic horseshoe vortices which are typically shed by fluttering membranes as seen in Huang and Sung (2010). FIG. 4 shows these horseshoe vortices are the result of leakage flow around the sides of the streamwise membrane edges on each side of the flag, which results from the pressure difference on the two sides of the flapping flag. The vortices generated from the edges of the membrane are mirrored across the midplane of the flag, and once they are shed, they induce the jetting behavior that leads to the swirl patterns seen in FIG. 3.

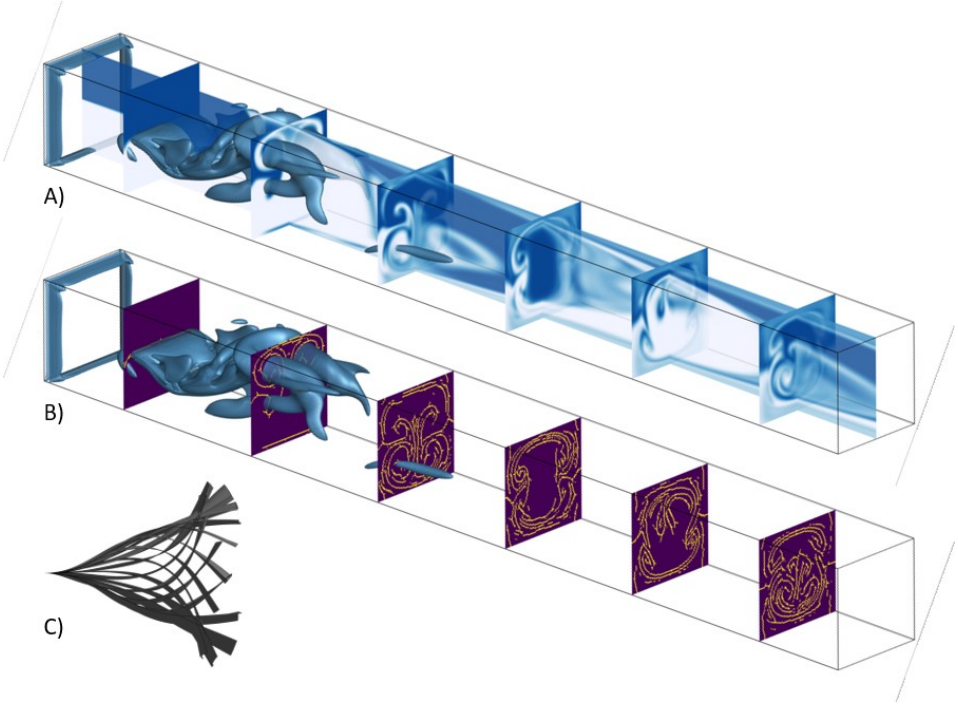

FIG. 3 – 3D visualizations of A) scalar concentration ϕ, B) the Interface Field ζ, and C) a sideview of the flapping envelope for the Re=200 case at one time-instance. The isosurfaces in the flow show vortices identified via the λ_2 vortex identification criterion (Jeong & Hussain, 1995). The λ_2 value for this isosurface is 1.6 L/U.

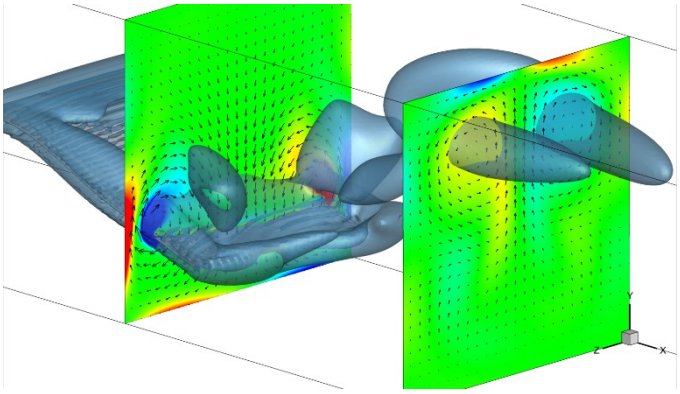

FIG. 4 – Zoomed in 3D snapshot of the Re=200 case showing the ω_z component of vorticity, the λ_2 criterion, and vector arrows showing the in-plane fluid velocity vectors (λ_2 = 2.5 L/U).

There appears to be two major benefits of the jets created by these vortices. First, the advection of fluid from one half of the duct into the other half is of crucial importance to mixing. Second, we can see at the centers of these vortices a clear swirl pattern of alternating light and dark-colored fluid. The effect of this can be seen more clearly by examining FIG. 3 where we can clearly see densely packed interfaces. This swirl pattern is beneficial in that it rapidly increases the interface length in the flow. It also tightly packs these striations, meaning that very quickly there will be pockets of very well mixed fluid.

In FIG. 3, we can see the continuation of this jetting process further downstream. By the next cross stream plane, we can see there are two halves of the jet, after splitting due to impinging on the upper (or lower) duct walls. By this point those half jets, which are made up of very thin layers of alternating scalar, re-collide in the middle of the duct. In the next plane, and the subsequent planes as well, we can see a pattern emerging wherein the area along the edges of the duct has much higher concentration of interfaces and is subsequently much more mixed than the fluid in the core of the duct which appears to have an oscillatory pattern. This examination provides a clear phenomenological view of how the production of streamwise vortices plays a crucial role in the creation of the highly stratified, well mixed layers along the duct walls.

4.1 Effect of Reynolds Number

The inertial microfluidics regime of Re=O(1-100) is unique in that both viscosity and inertia play an important role in the dynamics of the flow. This is especially true for systems which rely on vorticity, because the generation and persistence of vortices changes significantly in this Reynolds number regime. By examining the behavior of this system at a few Re numbers, namely Re=50, 100, 150, and 200, we can characterize the effects of this Reynolds number sensitivity. For these studies, Sc=100, flag length is L and the spanwise gap on either side is 0.125L (i.e. the flag aspect ratio is 0.75).

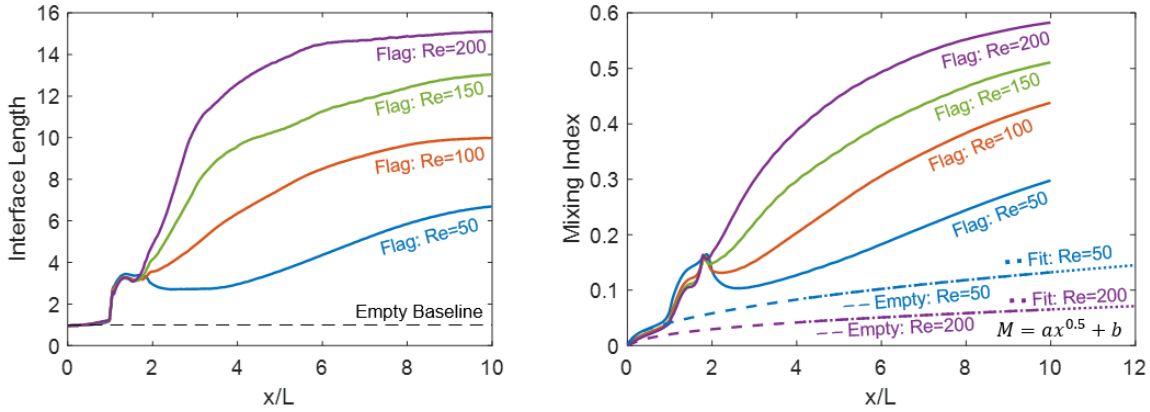

FIG. 5 – Time average of Normalized Interface Length (Left) and Mixing Index (Right) as a function of x/L for the four Re numbers simulated. Included in the Mixing Index plots are power-law regression curves for the empty duct cases, which are used in estimating the equivalent mixing length (E_M).

FIG. 5 shows the time-averaged normalized Interface Length I* and the Mixing Index M performance measures as a function of streamwise position x/L for each of the Re cases. Results for the empty duct at Re=50 and 200 are also included as a baseline for comparison. For both performance measures we can see a very strong dependence on the Reynolds number. For Re=50, the increase in interface length at x/L=10 is about a factor of 6.7 and thus, the flag stretches the interface by this factor at the exit of the duct. With increasing Re, the interface stretches even more dramatically and reaches a value of 15.1 for Re=200. All the interface length curves exhibit an asymptotic behavior indicating that beyond a certain distance downstream there is a cessation in the continuous stretching and folding of the interfaces. The Re=200 case, reaches this plateau by about x/L=6, whereas for lower Reynolds numbers, stretching and folding of the interface continues until about x/L=10. This cessation is due to the complete dissipation of the vortices which are responsible for the deformation of the fluid interface.

The Mixing Index plot shows the same strong Reynolds number dependence that was seen with the Interface Length. However, the Mixing Index plots exhibit a continuous increase with streamwise distance. This is expected since mixing is a result of the combined effect of stretching and folding (i.e. advection) as well as molecular diffusion. Thus, even after the cessation of stretching and folding exhibited beyond x/L=6 for the Re=200 case, molecular diffusion continues to mix the two scalar fields. The flutter mixer achieves mixing rates that up to about 58% after only 10 x/L of duct length for the Re=200 case, compared to just 6.5% for the duct without the flag at this Reynolds number.

Reynolds Number	Interface Length I*(10)	Mixing Index M(10) [M(10) for empty duct]	Equivalent Mixing Length (E_M)
50	6.7	0.30 [0.134]	50 L
100	10.0	0.44 [0.094]	214 L
150	13.1	0.51 [0.074]	509 L
200	15.1	0.58 [0.065]	835 L

Table 1: Normalized Interface length, Mixing Index, Equivalent Mixing Length for all the cases corresponding to FIG. 5.

One key design objective for a small-scale mixer is compactness, i.e. achieving the required degree of mixing in the smallest device size possible. In this regard it would be useful to assess the compactness afforded by the flutter mixer. One way to determine this is to estimate the length of the duct mixer without the flag that would result in the same level of mixing that the flutter mixer achieves at x/L=10. To

estimate this quantity, we fit a power-law curve to the Mixing Index curve of the empty duct (see Fig. 5). We find that except for in the entrance region, the Mixing Index in the empty duct (i.e. no flag) is very accurately (R^2=1.0000) modeled as a square root profile, i.e. $M(x) = a\,x^{0.5} + b$, where *a* and *b* depend on the Reynolds number (see FIG. 5B). Extrapolating from this power-law, we can estimate for each case with the flag, an equivalent length (E_M) of the empty duct (i.e. duct without a flag) that would achieve the same Mixing Index as the mixer with the flag at x/L=10. This equivalent mixing length is tabulated in Table 1 and it ranges from 50L for Re=50 to 835L for Re=200. This provides a clear view of the two to three orders of magnitude "compactness" in a mixer that would be enabled by the introduction of the flag. The equivalent length also provides a standard measure for normalized performance comparison across all types of mixers.

Our examination of the vorticity field for all the cases indicates that the Re=50 case is quite different from the other higher Reynolds number cases. We therefore examine this case in more detail to better understand why the performance degrades at lower Reynolds numbers. We find that while the Re=200 as well as the Re=100 and 150 cases (not shown here) all exhibit the jetting behavior, the Re=50 case does not. In FIG. 6 we show the vortex structures and interface plots for the Re=50 case, which shows this difference is due to the fact that the Re=50 case does not generate strong streamwise vortices, nor does it shed any vortices into the wake. Rather, the primary mechanisms for interface stretching in this case is the periodic upward and downward deformation of the interface due to the motion of the flag. It is clear from 6C that the amplitude of flutter is much lower for this case as compared to Re=200 and this along with the higher viscous dissipation, is responsible for the reduced mixing performance of this case.

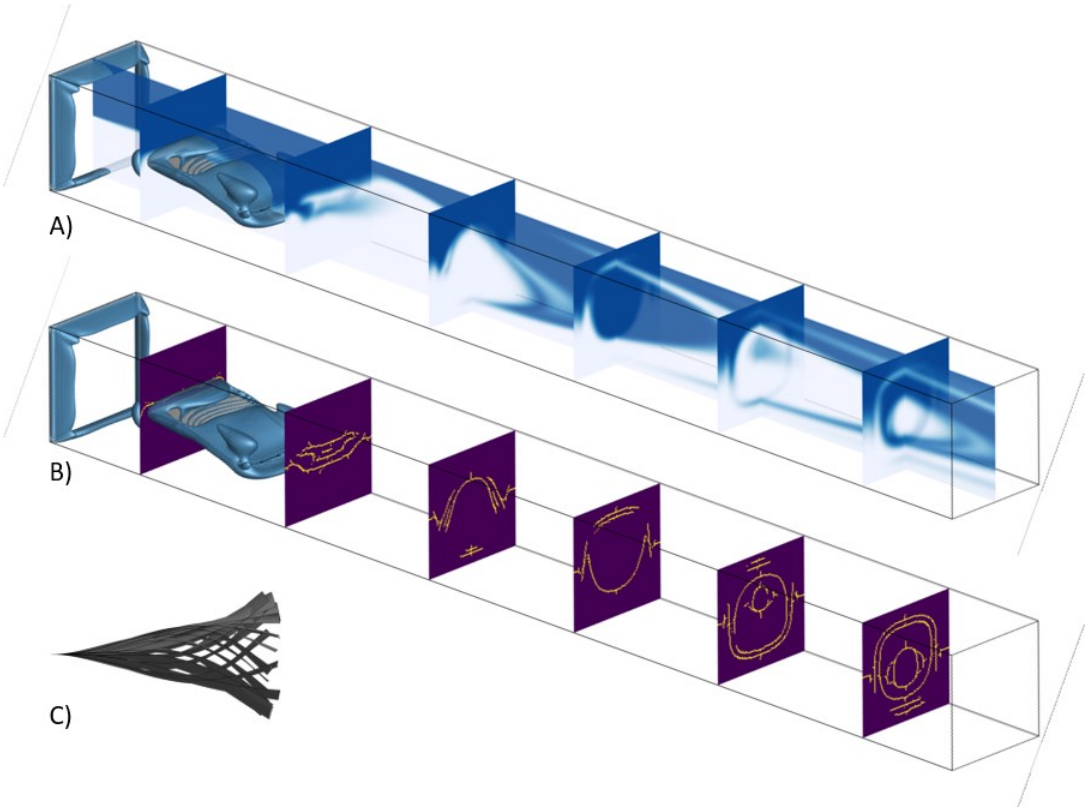

FIG. 6 – 3D visualizations of snapshots of A) scalar concentration ϕ , B) the Interface Field ζ for the AR=0.75, Re=50 case. C) Flag flutter envelope. The isosurfaces in the flow show the λ_2 vortex identification criterion (λ_2 = 1.6 L/U).

To better understand the effect of the Reynolds number on the performance of these mixers, we turn our attention to the dynamics of the flags. FIG. 7 summarizes the effect of Reynolds number on the amplitude, frequency (Strouhal number defined as St=fL/U), and mode-shape of the flags. In general, we can see increasing amplitudes and decreasing flapping frequency with increasing Re. This is in line with the behavior noted in the 2D simulations of Rips & Mittal (2019). However, from Re=50 to Re=100, there is a more significant jump in both the amplitude and the Strouhal number, with the subsequent Reynolds number cases showing smaller changes. Interestingly, there is no significant difference in the mode shapes of the flags with the Reynolds number. Furthermore, for all the cases, the flag exhibits noticeable but low levels of spanwise bending.

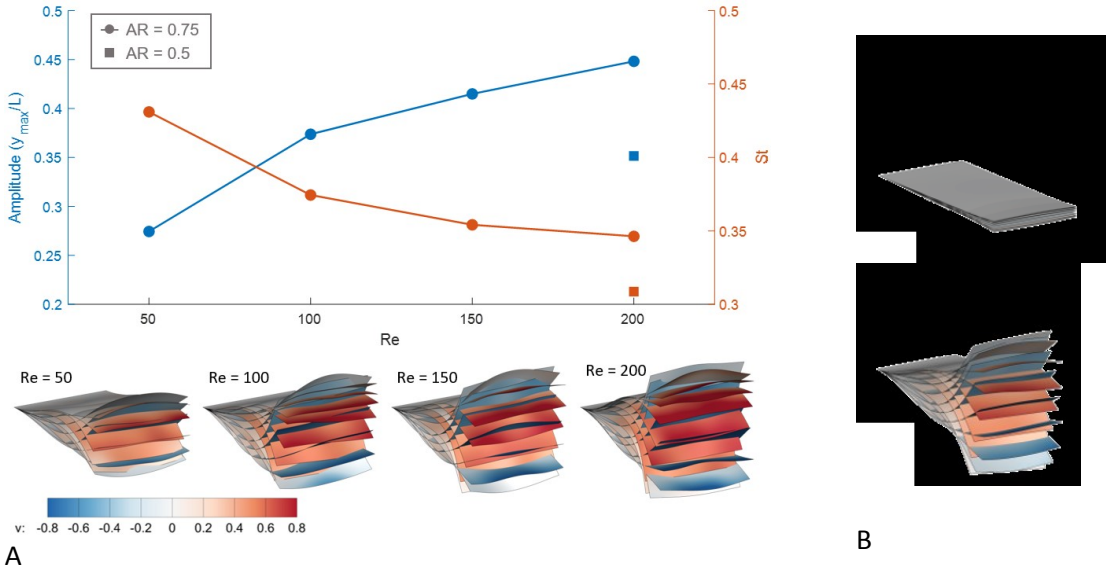

FIG. 7 – A. Flapping dynamics for the 3D flag as a function of Re showing flapping half amplitude and the Strouhal number. Bottom of the figure shows 3D views of the flapping envelopes for the AR=0.75 flag showing approximately one flapping cycle. The color contours on the membrane surfaces show the local y component of the flag's velocity, providing a sense of what direction each snapshot is traveling. B. envelopes for the AR=0.5 case at two Reynolds numbers.

4.2 Flag Aspect-Ratio and Spanwise Confinement

As is evident from the previous discussion, the streamwise vortices formed at the edges of the flag play a crucial role in the stretching and folding of the fluid interface. The formation of the streamwise vortices is in turn expected to vary with the spanwise aspect ratio as well as the spanwise confinement of the flag. Indeed, both of these parameters have been shown in prior work (Doaré et al., 2011; C. Eloy, Souilliez, & Schouveiler, 2007) to affect the dynamical stability the flags. Our initial tests indicated that thin flags (AR<0.5) flap with a much-reduced amplitude and also do not generate strong vortex structures for mixing. We therefore focused on an intermediate value of aspect ratio (AR=0.5) which was large enough to generate strong flapping but different enough from the AR=0.75 case so as to enable some useful insights. For this AR, we conducted simulations at two Reynolds numbers: Re=50 and Re=200. It turns out however, that the AR=0.5 flag does not exhibit any significant flapping at Re=50 (see Fig. 7B) and therefore has poor mixing performance. We therefore focus on describing the dynamics of the AR=0.5; Re=200 case and FIG. 7 includes the flutter characteristics for this case. The behavior for the AR=0.5 case appears generally similar to the AR=0.75 case, however, this case has a smaller Strouhal number and a smaller

flapping amplitude. This change in flag dynamics points to the importance of finite-span and spanwise confinement effects on the membrane dynamics. In particular, our results are consistent with Eloy (2007), who showed that decreasing aspect-ratio tends to stabilize flag flutter.

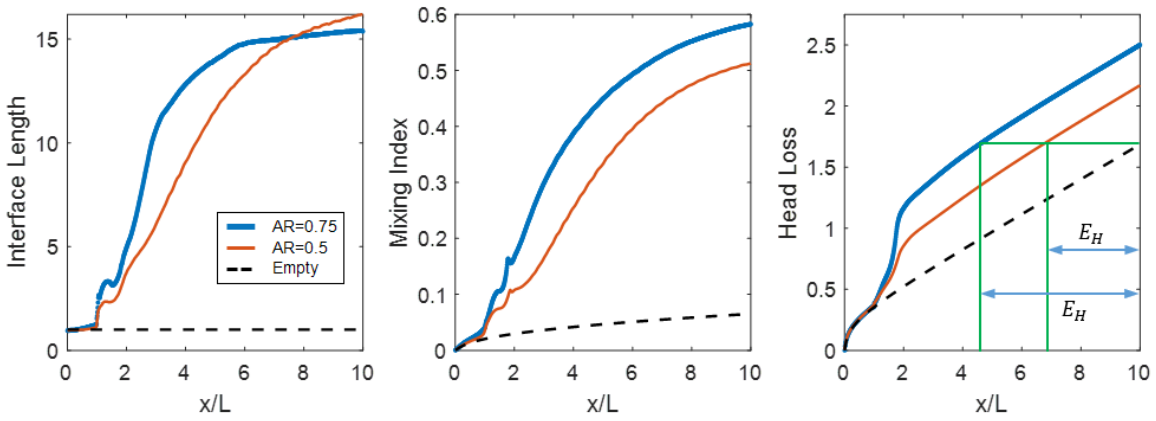

FIG. 8 – Time average of the Normalized Interface Length, Mixing Index, and Head Loss as a function of x/L for the AR = 0.75 and AR = 0.5 cases and the empty duct baseline all at Re=200. Table shows Mixing Index and Head Loss measures which lead to the Coefficient of Performance.

FIG. 8 shows the performance comparison between the AR=0.5 and AR=0.75 cases in terms of the interface length, mixing index, and head loss. The results indicate that the AR=0.5 aspect-ratio case shows a much slower initial rise in the interface length with downstream distance compared to the AR=0.75 case. However, the interface length in the AR=0.5 continues to increase and exceeds the value for the AR=0.75 case at about x/L=7.5. The plot of the Mixing Index shows that the AR=0.5 case lags behind the AR=0.75 in this measure, and this is expected given the more rapid rise of the interface length in the latter case. However, it is expected that the AR=0.5 case will match and maybe even exceed the Mixing Index further downstream given that it generates greater stretching and folding of the interface. The equivalent mixing length for the AR=0.5 flutter mixer is about 637, which although large, is still smaller than that for the AR=0.75 mixer.

Flag Aspect Ratio (W/L)	Mixing Index M(10)	Mixing Equivalent Length (E_M)	Head Loss Equivalent Length (E_H)	Coefficient of Performance (CoP=E_M/E_H)
0.75	0.58	825	5.4	152
0.5	0.51	637	3.3	195

Table 2 Mixing and Head Loss measures for the two different aspect ratio flags.

Fig. 8 indicates that the AR=0.5 case generates a lower loss in mechanical energy than the AR=0.75 case. This is expected since the loss in mechanical energy is associated with the viscous drag on the membrane as well as the work done by the flow in deforming the elastic membrane. Both are proportional to the area of the membrane, which is larger for the AR=0.75 case. A practical and well-established way of assessing minor head-losses is to estimate the equivalent length (E_H) of the duct without the membrane, which would incur the same head loss as that due to the membrane (see FIG. 8). The head loss in the duct without the flag is linear and using this, we find that the additional losses for the AR=0.75 membrane are equivalent to a duct length of 5.4L and the AR=0.50 membrane generated losses equivalent to a duct length of 3.3L**.** However, as is clear from the plot of the Mixing Index in FIG. 8 that such a small increase in the length of the duct would have no noticeable effect on the mixing in the empty duct. Indeed, one

can define a Coefficient of Performance (CoP) for the mixer as a ratio of the equivalent lengths for mixing and head loss (i.e. $CoP=E_M/E_H$), and this provides a useful measure of the increase in mixing relative to the increase in head loss for a given mixer, in comparison to a baseline design. The value of this coefficient is 152 for the AR=0.75 case and 195 for the AR=0.5 case, indicating that when indexed for the mechanical energy loss, the AR=0.5 mixer provides an overall better mixing performance.

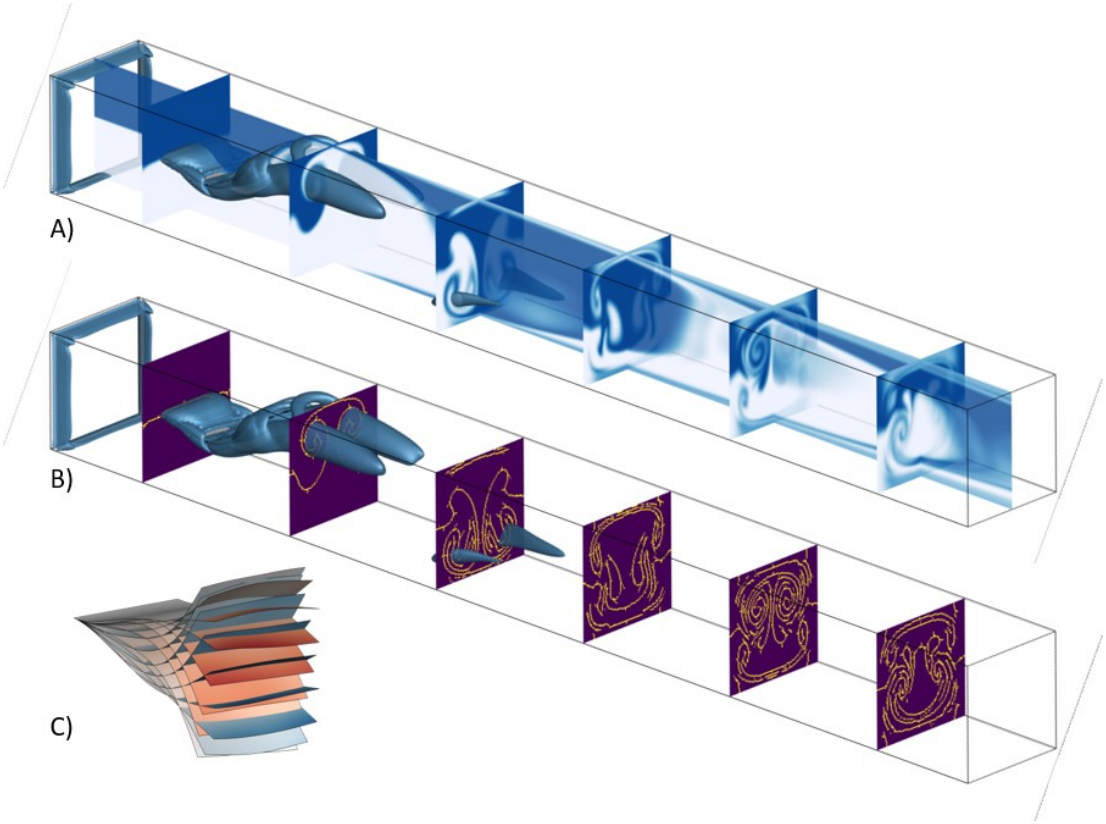

FIG. 9 – 3D visualizations of snapshots of A) scalar concentration ϕ, B) the Interface Field ζ for the AR=0.5, Re=200 case. C) shows snapshots of the flapping envelope for the AR=0.5 membrane (λ_2 = 1.6L/U).

FIG. 9 shows the vortex pattern for the AR=0.5 case and this can be compared directly to the corresponding figure for the AR=0.75 case (FIG. 3). The vortex patterns for the two share some similarities but the one key difference is the dominance of streamwise vortices in the wake of the AR=0.50 case. In contrast, the AR=0.75 case shows a more complex topology with strong spanwise oriented vortices also being formed and interacting with the streamwise vortices. This is because the spanwise oriented vortices are generated at the trailing edge of the membrane, which is larger for the AR=0.75 case.

This difference in vortex topology provides a qualitative explanation for the trend observed in the interface length plot for these cases. The formation of complex spanwise vortices in the AR=0.75 cases results in rapid initial mixing, but it also leads to faster dissolution of the streamwise vortices. In contrast, for the AR=0.50 case, the weak spanwise vortices do not contribute much to the initial stretching and folding of the fluid interface. However, a collateral consequence is that the streamwise vortices are not deformed by the mutual induction with the spanwise vortices; they therefore manage to persist much longer and continue to deform and elongate the fluid interface for a greater streamwise distance. Overall, the above results indicate that it may be possible to select membrane configurations that can significantly

enhance mixing while at the same time limiting the overall pressure losses by maximizing the ratio of streamwise to spanwise vorticity production.

5 Conclusion

In this study we have examined flow-induced flutter of a membrane as a mechanism for enhancing mixing in a small-scale mixer. Using fully coupled fluid-structure-scalar interaction simulations we investigated in detail the structural dynamics of this flutter behavior and the resulting flow and scalar transport created by the flapping motion. We then examined how the flow and the vorticity field gives rise to the significant mixing improvement and employed a new metric that estimates the length of the interface generated by vortex-induced stretching and folding. The simulations were also used to examine the changes in mixer performance with Reynolds number as well as the membrane aspect-ratio. We showed a strong dependence of the system on the Reynolds number. These results show that these flutter mixers can achieve very rapid mixing in the region immediately downstream of the membrane. By employing equivalent length parameters for both mixing as well as the head loss, we quantified both the compactness afforded by the flutter mixers and the energy efficiency of different mixer designs. The study suggests that these flutter mixers can enable a high degree of mixing in compact devices, and system parameters might be optimized to provide high mixing for low attendant pressure losses.

6 Acknowledgement

The development of the FSI Solver benefitted from support from NSF grant PHY180668.

References

Afzal, A., & Kim, K. (2012). *Passive split and recombination micromixer with convergent–divergent walls* doi://doi.org/10.1016/j.cej.2012.06.111

Alben, S. (2015). Flag flutter in inviscid channel flow. *Physics of Fluids, 27*(3), 033603. doi:10.1063/1.4915897

Amini, H., Lee, W., & Di Carlo, D. (2014). Inertial microfluidic physics. *Lab on a Chip, 14*(15), 2739-2761. doi:10.1039/c4lc00128a

Cai, G., Xue, L., Zhang, H., & Lin, J. (2017). A review on micromixers. *Micromachines, 8*(9), 274.

Capretto, L., Cheng, W., Hill, M., & Zhang, X. (2011). Micromixing within microfluidic devices. *Microfluidics* (pp. 27-68) Springer.

Doaré, O., Sauzade, M., & Eloy, C. (2011). Flutter of an elastic plate in a channel flow: Confinement and finite-size effects. *Journal of Fluids and Structures, 27*(1), 76-88. doi:10.1016/j.jfluidstructs.2010.09.002

Eloy, C., Souilliez, C., & Schouveiler, L. (2007). *Flutter of a rectangular plate* doi://doi.org/10.1016/j.jfluidstructs.2007.02.002

ELOY, C., LAGRANGE, R., SOUILLIEZ, C., & SCHOUVEILER, L. (2008). Aeroelastic instability of cantilevered flexible plates in uniform flow. *Journal of Fluid Mechanics, 611*, 97-106. doi:10.1017/S002211200800284X

Fox, Robert W.,, Pritchard, Philip J., McDonald,Alan T.,. (2011). *Fox and McDonald's introduction to fluid mechanics.* Hoboken, NJ; Chichester: John Wiley & Sons, Inc. ; John Wiley [distributor].

Hossain, S., Ansari, M. A., & Kim, K. (2009). Evaluation of the mixing performance of three passive micromixers. *Chemical Engineering Journal, 150*(2-3), 492-501.

Huang, W., & Sung, H. J. (2010). Three-dimensional simulation of a flapping flag in a uniform flow. *Journal of Fluid Mechanics, 653*, 301-336.

Jeong, J., & Hussain, F. (1995). On the identification of a vortex. *Journal of Fluid Mechanics, 285*, 69-94. doi:10.1017/S0022112095000462

Lee, C., Chang, C., Wang, Y., & Fu, L. (2011). Microfluidic mixing: A review. *International Journal of Molecular Sciences, 12*(5), 3263-3287.

Lee, C., Wang, W., Liu, C., & Fu, L. (2016). *Passive mixers in microfluidic systems: A review* doi://doi.org/10.1016/j.cej.2015.10.122

Mittal, R., Dong, H., Bozkurttas, M., Najjar, F. M., Vargas, A., & von Loebbecke, A. (2008). A versatile sharp interface immersed boundary method for incompressible flows with complex boundaries. *Journal of Computational Physics, 227*(10), 4825-4852.

Nguyen, N., & Wu, Z. (2004). Micromixers—a review. *Journal of Micromechanics and Microengineering, 15*(2), R1.

Rips, A., & Mittal, R. (2019). Enhanced mixing at inertial microscales using flow-induced flutter. *Physical Review Fluids, 4*(5), 054501.

Rips, A., Shoele, K., Glezer, A., & Mittal, R. (2017). (2017). Efficient electronic cooling via flow-induced vibrations. Paper presented at the *Thermal Measurement, Modeling & Management Symposium (SEMI-THERM), 2017 33rd,* 36-39.

Seo, J. H., & Mittal, R. (2011). A sharp-interface immersed boundary method with improved mass conservation and reduced spurious pressure oscillations. *Journal of Computational Physics, 230*(19), 7347-7363.

Shoele, K., & Mittal, R. (2014). Computational study of flow-induced vibration of a reed in a channel and effect on convective heat transfer. *Physics of Fluids, 26*(12), 127103. doi:10.1063/1.4903793

Shoele, K., & Mittal, R. (2016). Energy harvesting by flow-induced flutter in a simple model of an inverted piezoelectric flag. *Journal of Fluid Mechanics, 790*, 582-606.

Shoele, K., & Zhu, Q. (2012). Leading edge strengthening and the propulsion performance of flexible ray fins. *Journal of Fluid Mechanics, 693*, 402-432. doi:10.1017/jfm.2011.538

Stone, H. A., Stroock, A. D., & Ajdari, A. (2004). Engineering flows in small devices: Microfluidics toward a lab-on-a-chip. *Annu.Rev.Fluid Mech., 36*, 381-411.

Wang, X., Alben, S., Li, C., & Young, Y. L. (2016). Stability and scalability of piezoelectric flags. *Physics of Fluids, 28*(2), 023601. doi:10.1063/1.4940990

Zhang, J., Yan, S., Yuan, D., Alici, G., Nguyen, N., Warkiani, M. E., & Li, W. (2016). Fundamentals and applications of inertial microfluidics: A review. *Lab on a Chip, 16*(1), 10-34.

Zhu, C., Seo, J. H., Vedula, V., & Mittal, R. (2017). (2017). A highly scalable sharp-interface immersed boundary method for large-scale parallel computers. Paper presented at the *23rd AIAA Computational Fluid Dynamics Conference,* 3622.